3D Bioelectromagnetic Computation on Finite Elements

Keith D. Paulsen, Xilin Jia, and Daniel R. Lynch
Thayer School of Engineering
Dartmouth College, Hanover, NH, USA

Abstract

Finite element computation of electric and magnetic fields induced in the body by noninvasive electromagnetic sources is discussed. Attention is focussed on three-dimensional calculations for full-scale body models with significant levels of internal anatomical structure. The finite element solution strategy including the sparse matrix approach which allows computation of over 100K degrees-of-freedom on standard reduced instruction set computer (RISC) workstation platforms is outlined. The finite element mesh generation problem is also described. Representative examples of the level of meshing detail and the type of 3D bioelectromagnetic solutions that can be achieved using finite elements in the workstation computing environment are shown.

I. Introduction

The need to quantify induced electromagnetic (EM) field distributions in biological bodies arises in numerous medical and health-related contexts, for example, in microwave imaging for diagnosis [Larson and Jacobi,1986; Jofre *et. al.*, 1990], and in hyperthermia cancer therapy [Hand, 1990; *Int. J. Hyperthermia*, Special Issue, 1988], among others. Of primary concern has typically been the nature of the detailed EM field distributions created inside the body, knowledge of which is required to quantify dose delivery or characterize tissue. The large electrical contrast between many tissues in the frequency ranges of interest [Stuchly and Stuchly, 1980] and the complex geometry of the human anatomy has made determination of internal field distributions a challenging problem requiring state-of-the-art computational methods.

While a variety of approaches are proving successful in the bioelectromagnetics context (e.g. see [Gandhi, 1990; Paulsen, 1990]), the finite element method (FEM) is a natural choice because of its inherent ability to treat highly heterogeneous, irregularly-shaped computational domains. For example, in hyperthermia treatment planning for cancer therapy, 2D FEM modeling has proven to be quite informative [Strohbehn *et. al.* 1986]. Detailed EM field distributions and concomitant specific absorption rate (SAR) profiles have been calculated in 2D anatomical models derived from planar CT-scans of actual cancer patients. Comparisons have been made between various competing therapy devices [Paulsen *et. al.*, 1985] as well as with actual clinical data [Strohbehn *et. al.*, 1986; Paulsen and Ross, 1990] and the general trends predicted by these analyses have been borne out in clinical trials [Sapozink *et. al.*, 1985]. The success of this type of 2D modeling has provided a strong rationale for extending the computational capabilities to 3D for potential use in planning the treatments of individual patients [Sullivan, 1990; Piket-May *et. al.*, 1991]. Likewise, in other biomedical contexts the induced EM field distributions are essentially three-dimensional [Chen and Gandhi, 1989; Caorsi *et. al.* 1989]; thus, the need for 3D computational methods and algorithms is critical to the understanding of the interactions of EM fields with biological bodies and the advancement of biomedical applications of EM energy.

In this paper, we report on our progress in computing 3D EM field distributions in full-body models with the finite element method. While the specific examples we present are of primary interest in hyperthermic treatment of cancer, the methods and approaches we utilize are relevant to bioelectromagnetic computing in general. We begin by reviewing our basic FEM formulation for calculating EM fields in biological tissue; we discuss our iterative solution strategy, our sparse matrix storage structure and the problem sizes/run-times that we can achieve on a typical reduced instruction set computer (RISC) workstation. We also discuss the grid generation techniques we

employ and show examples of the type of meshes we can create. We conclude by showing some EM field calculations in full-body models with noninvasive current excitations which are of importance in hyperthermia treatment of cancer.

II. FEM Formulation

In this section we briefly recount our finite element approach [Paulsen and Lynch, 1991; Lynch and Paulsen, 1991; Boyse *et. al.*, 1992]. We use an "extended weak form" that produces a special Helmholtz structure on homogeneous subregions with component coupling occurring only at media interfaces and boundaries where boundary integrals arise in terms of naturally specifiable quantities. The advantages of this approach are (1) the ability to use conventional FEM scalar bases as expansion functions while simultaneously eliminating the parasitic behavior that can occur in the discrete form of the double-curl operator [Lynch and Paulsen, 1991; Boyse *et. al.* 1992] and (2) the enhanced sparsity of the system matrix as a by-product of the decoupling of interior field components [Paulsen and Lynch, 1991].

In contrast to most of our earlier work where we solve directly for the electric field $\mathbf{E}$, herein, we compute the magnetic field $\mathbf{H}$ and subsequently determine $\mathbf{E}$ from the $\nabla \times \mathbf{H}$ if and when it is needed. For the problems of interest in many biomedical applications, the magnetic permeability of tissue, μ , can be considered constant whereas the permittivity, ϵ, and conductivity, σ, both vary with tissue type and frequency. Under these assumptions, all components of $\mathbf{H}$ are continuous in source-free regions (i.e. inside the body) and the strong enforcement of EM jump conditions [Yuan *et. al.*, 1991] can be delayed until the subsequent calculation of $\mathbf{E}$.

The "extended weak form" for $\mathbf{H}$ can be obtained from the weighted residual statement

$$< \left(\nabla \times \frac{1}{i\omega\epsilon^*} \nabla \times \mathbf{H} - \nabla \left(\frac{1}{i\omega\epsilon^*\mu} \nabla \cdot \mu\mathbf{H} \right) + i\omega\mu\mathbf{H} \right) \phi_i >= 0 \tag{1}$$

where $\epsilon^* = \epsilon + i\sigma/\omega$ is the complex permittivity, $< >$ indicates volume integration over the problem domain, ϕ_i is the locally-defined linearly-varying weighting function associated with each finite element nodal position, and an $e^{-i\omega t}$ time-variation is implied. Use of standard vector identities and integral theorems allows one to remove the second order differentiation in favor of relevant boundary integrals

$$\left\langle \frac{1}{i\omega\epsilon^*} \nabla \times \mathbf{H} \times \nabla\phi_i \right\rangle + \left\langle \frac{1}{i\omega\epsilon^*\mu} (\nabla \cdot \mu\mathbf{H}) \nabla\phi_i \right\rangle + \langle i\omega\mu\mathbf{H}\phi_i \rangle =$$

$$- \oint \hat{\mathbf{n}} \times \left(\frac{1}{i\omega\epsilon^*} \nabla \times \mathbf{H} \right) \phi_i \, ds + \oint \hat{\mathbf{n}} \frac{1}{i\omega\epsilon^*\mu} (\nabla \cdot \mu\mathbf{H}) \phi_i \, ds \tag{2}$$

A symmetric linear algebraic system of equations $\mathbf{Ax} = \mathbf{b}$ is generated by expanding $\mathbf{H} = \sum_{j=1}^{N} \mathbf{H}_j \phi_j$ in the usual Galerkin fashion which leads to $\mathbf{A}$ being composed of the complex submatrices

$$\mathbf{A}_{ij} = \begin{pmatrix} \langle \frac{1}{i\omega\epsilon^*}(\frac{\partial\phi_j}{\partial y}\frac{\partial\phi_i}{\partial y} + \frac{\partial\phi_j}{\partial z}\frac{\partial\phi_i}{\partial z} + \frac{\partial\phi_j}{\partial x}\frac{\partial\phi_i}{\partial x})\rangle + \langle i\omega\mu\phi_i\phi_j\rangle & \langle \frac{1}{i\omega\epsilon^*}(-\frac{\partial\phi_j}{\partial x}\frac{\partial\phi_i}{\partial y} + \frac{\partial\phi_j}{\partial y}\frac{\partial\phi_i}{\partial x})\rangle & \langle \frac{1}{i\omega\epsilon^*}(-\frac{\partial\phi_j}{\partial x}\frac{\partial\phi_i}{\partial z} + \frac{\partial\phi_j}{\partial z}\frac{\partial\phi_i}{\partial x})\rangle \\ \langle \frac{1}{i\omega\epsilon^*}(-\frac{\partial\phi_j}{\partial y}\frac{\partial\phi_i}{\partial x} + \frac{\partial\phi_j}{\partial x}\frac{\partial\phi_i}{\partial y})\rangle & \langle \frac{1}{i\omega\epsilon^*}(\frac{\partial\phi_j}{\partial x}\frac{\partial\phi_i}{\partial x} + \frac{\partial\phi_j}{\partial z}\frac{\partial\phi_i}{\partial z} + \frac{\partial\phi_j}{\partial y}\frac{\partial\phi_i}{\partial y})\rangle + \langle i\omega\mu\phi_i\phi_j\rangle & \langle \frac{1}{i\omega\epsilon^*}(-\frac{\partial\phi_j}{\partial y}\frac{\partial\phi_i}{\partial z} + \frac{\partial\phi_j}{\partial z}\frac{\partial\phi_i}{\partial y})\rangle \\ \langle \frac{1}{i\omega\epsilon^*}(-\frac{\partial\phi_j}{\partial z}\frac{\partial\phi_i}{\partial x} + \frac{\partial\phi_j}{\partial x}\frac{\partial\phi_i}{\partial z})\rangle & \langle \frac{1}{i\omega\epsilon^*}(-\frac{\partial\phi_j}{\partial z}\frac{\partial\phi_i}{\partial y} + \frac{\partial\phi_j}{\partial y}\frac{\partial\phi_i}{\partial z})\rangle & \langle \frac{1}{i\omega\epsilon^*}(\frac{\partial\phi_j}{\partial x}\frac{\partial\phi_i}{\partial x} + \frac{\partial\phi_j}{\partial y}\frac{\partial\phi_i}{\partial y} + \frac{\partial\phi_j}{\partial z}\frac{\partial\phi_i}{\partial z})\rangle + \langle i\omega\mu\phi_i\phi_j\rangle \end{pmatrix} \tag{3}$$

Boundary conditions are handled through the surface integrals appearing on the right-side of (2). When tangential $\mathbf{E}$ is specified, the first boundary integral is computed as the driving term for the tangential components of (2) while the normal component of (2) is discarded in favor of the known value of H_n (i.e. $\hat{\mathbf{n}}\cdot\mathbf{H} = \frac{-1}{i\omega\mu}\hat{\mathbf{n}}\cdot\nabla\times\mathbf{E}$). For boundaries where tangential $\mathbf{H}$ is specified, the tangential components of (2) are removed in favor of the known information whereas the normal component of (2) is enforced with homogeneous conditions (i.e. the second boundary integral in (2) vanishes). Finally, we implement current sources, if present, through strong enforcement of a jump condition on the tangential components of $\mathbf{H}$ at a current-carrying boundary:

$$\hat{\mathbf{n}}\times(\mathbf{H}_1 - \mathbf{H}_2) = \mathbf{J} \tag{4}$$

At such nodal locations, $\mathbf{H}$ has two computed values whose appropriate components are made to be discontinuous by the known amount of $\mathbf{J}$.

III. Sparse Matrix Solution

We solve the sparse set of algebraic equations generated by our FEM procedure with a symmetric, preconditioned form§ of the Biconjugate Gradient Method (BCG)[Freund 1992]. Whenever i or j in (3) are not on a boundary or interface we save only 3 memory locations for the diagonal elements (all others vanishing on the elements we employ [Paulsen and Lynch, 1991]). For (i,j) combinations where both are on the boundary/interface, space is reserved for the full 3×3 submatrix in (3). With this memory economization, we have been able to compute solutions on meshes with more than 100K degrees-of-freedom using an IBM RS6000 series platform. Run-times have been on the order of 3-8 hours depending on the number of iterations consumed during a given solution. We monitor the equation residual, $||\mathbf{r}_i||_2 = ||\mathbf{b} - \mathbf{A}\mathbf{x}_i||_2$, for each iteration $i = 1, 2\ldots$, and use this information as a measure of convergence. Typically, we normalize the initial equation residual (using an initial guess equal to the right-hand-side forcing vector) to unity and iterate until the initial equation residual has been reduced 3-4 orders of magnitude. In some of our longer runs (i.e. 8 hrs) we have used the stopping criterion of 2500 total iterations rather than terminating the solution when the equation residual has reached a prescribed value.

Because the equation residual for the BCG is not monotonic in its decent [Freund, 1992], choosing a definitive stopping rule has not been obvious. For problems with analytic solutions we have tracked both the equation residual and the solution residual (i.e. $||\mathbf{r}_i||_2 = ||\mathbf{x}_i - \mathbf{x}_{analytic}||_2$) and found a strong correspondence between the two. Figures 1a-b show the equation and solution residuals as functions of iteration for small homogeneous sphere problems ($\approx$ 9–28K degrees-of-freedom) where we have imposed boundary conditions on tangential $\mathbf{H}$ at the outer sphere surface, namely

§ We use right ILU preconditioning [Langtangen, 1989] with matrix reordering [George and Liu, 1981]

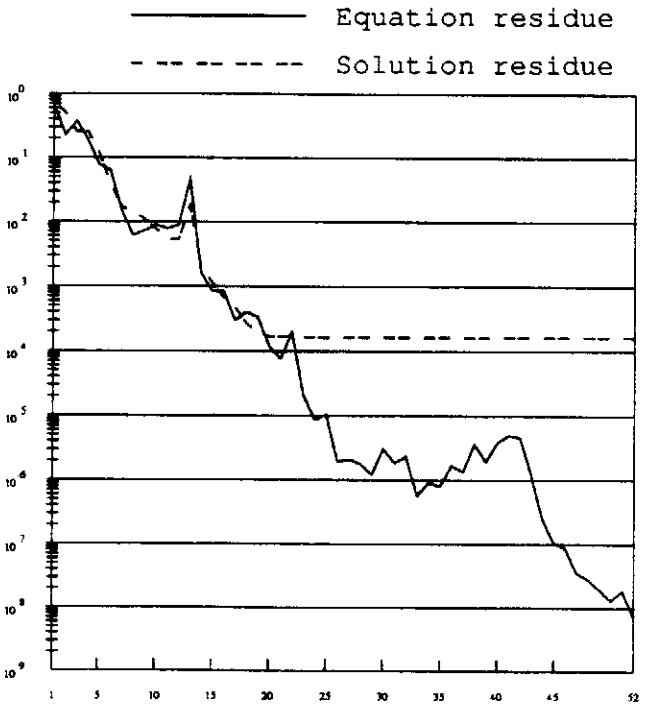

Figure 1a: Normalized solution and equation residuals as functions of iteration for a small sphere problem of 3144 nodes where an analytic solution exists.

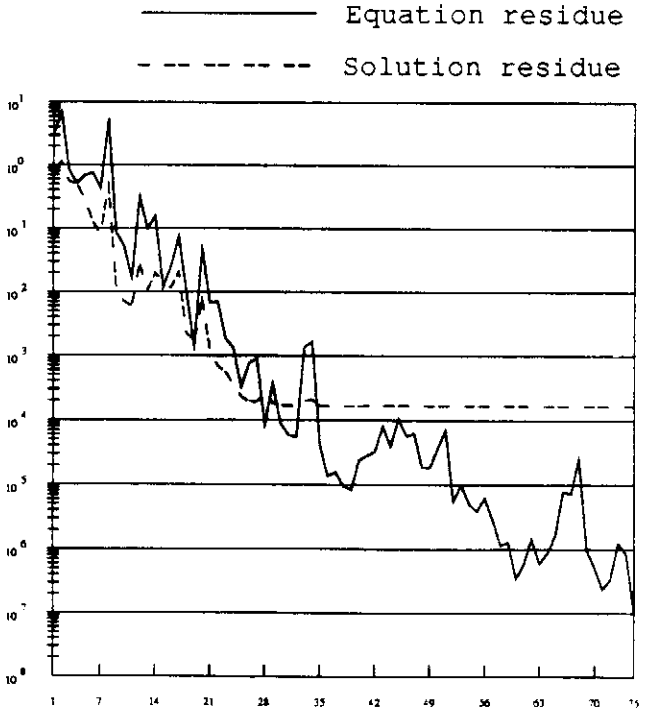

$\mathbf{H} = sin(\theta)\hat{\phi}$. The radius of the sphere used in these figures was 0.2 meters and its electrical properties were $\epsilon_r = 20$, $\sigma = 0.01\,\Omega^{-1}m^{-1}$ The frequency of excitation was 70MHz. Note that the normalized solution residual does not decrease below 10^{-4} because only 4 significant figures

from the analytic solution were used in the comparisons. The behavior displayed in these plots is characteristic of the numerous sphere calculations we have made of this type. We find the solution accuracy is excellent for an equation residual which has been reduced 3-4 orders of magnitude from its initial value. Figure 1c shows that the computed **H** is essentially indistinguishable from the analytic solution for this level of convergence. Further, in nonanalytic cases (i.e. full-body models of the type we present in Section V) we have used a "converged" iterative solution† as the "analytic" solution needed to compute the solution residual and have studied the behavior of the equation residual relative to this solution residual as a function of iteration count.

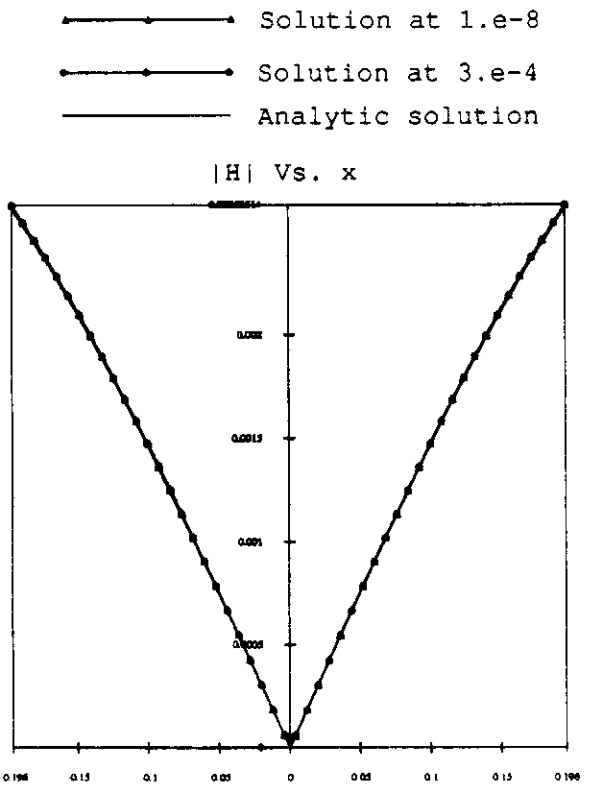

Figure 1c: Iterative **H** calculations with normalized equation residuals reduced to 10^{-4} and 10^{-8} compared to the analytic solution. Curves show magnitude as a function of radius for a homogeneous sphere with $\epsilon_r = 20$ and $\sigma = 0.1\,\Omega^{-1}m^{-1}$.

A sample result is displayed in Figure 1d. Again, we found a strong correspondence between the two with the caveat that some early dips (within the first 100 iterations) in the equation residual often do not relate to decreases in the solution residual. Based on our experiences we believe a 3-4 orders of magnitude decrease in the initial equation residual is a reliable stopping criterion; however, as a conservative measure the solutions we report below have been iterated a fixed number (2500) of times and have equation residuals near 10^{-5}.

IV. Mesh Generation

One of the more challenging problems in using finite element analysis in 3D bioelectromagnetic applications is the generation of the FEM mesh. This is especially true if one wishes to take advantage of the real power of the method by using variable element sizes and faithful representations of the anatomical geometry of interest. Since in many biomedical contexts anatomical structure

† One with a normalized equation residual reduced to 10^{-5}

is available through serial CT-scans (this is certainly the case in hyperthermia cancer therapy), we begin the process of mesh generation by identifying the organs and tissues of interest on each CT-scan. The individual contours on each CT-slice are then linearly interpolated in the third dimension which produces a boundary element description of the anatomical model. Figure 2 shows a sample boundary description of a typical full-body anatomy which is to be meshed. We do not require that the actual nodes and surface elements shown in Figure 2 be part of the final FEM mesh, but only that the boundaries of the final FEM mesh conform to those displayed in the figure.

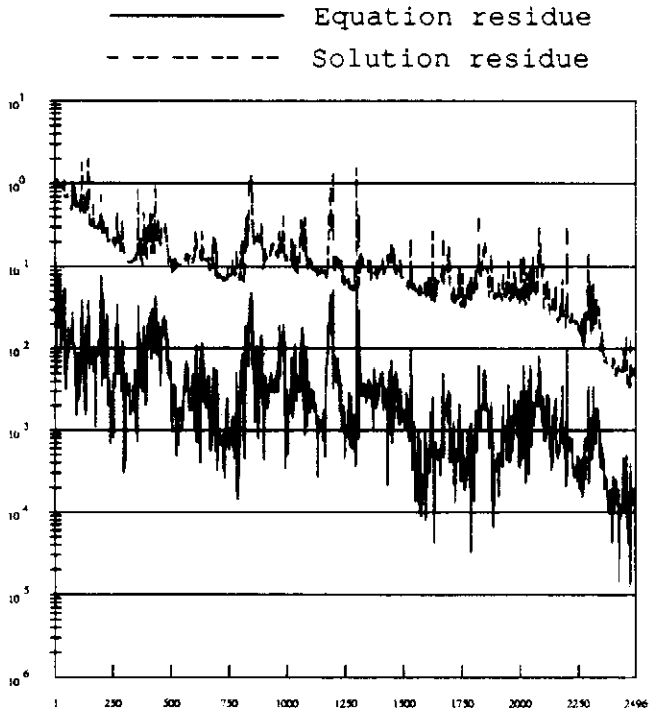

Figure 1d: Normalized solution and equation residuals as functions of iteration for a large full-body model ($\approx$ 135K degrees-of-freedom).

To generate the tetrahedral elements which are to fill the volume specified while simultaneously conforming to the boundaries delineated we use the nodal-pulling algorithm of Sullivan and Charron (1991). This is essentially the 3D version of a 2D mesh generator we have used successfully in the past [Lynch *et. al.*, 1987]. The strategy is to initially deploy the nodes and elements on a uniform lattice and to distort this lattice near the boundaries by pulling the nodes nearest to the predefined boundaries onto those boundaries. Localized refinements are possible over selected portions of the domain and result in a reduction in the characteristic nodal spacing by a factor of two for each refinement. Hence, the user specifies the largest mesh spacing that is to exist within the mesh as a starting gauge and subsequently refines the mesh in the appropriate areas until the desired resolution is achieved. During the entire process the nodal placement is continually altered near the boundaries such that the boundaries of the final mesh conform to those of the initially defined geometry. Figure 3 shows a sample mesh generated in this fashion. For ease of viewing and comparison with the initial boundary description (Figure 2) only the boundaries of the final mesh are displayed. It is clear from Figure 3 that several refinements have taken place in the areas of the most significant geometric detail. The final volume mesh for Figure 3 has 45K nodes (135K degrees-of-freedom) and 251K tetrahedral elements. To compute a solution on this mesh using a RISC workstation, our sparse matrix method (including auxiliary arrays and the preconditioner

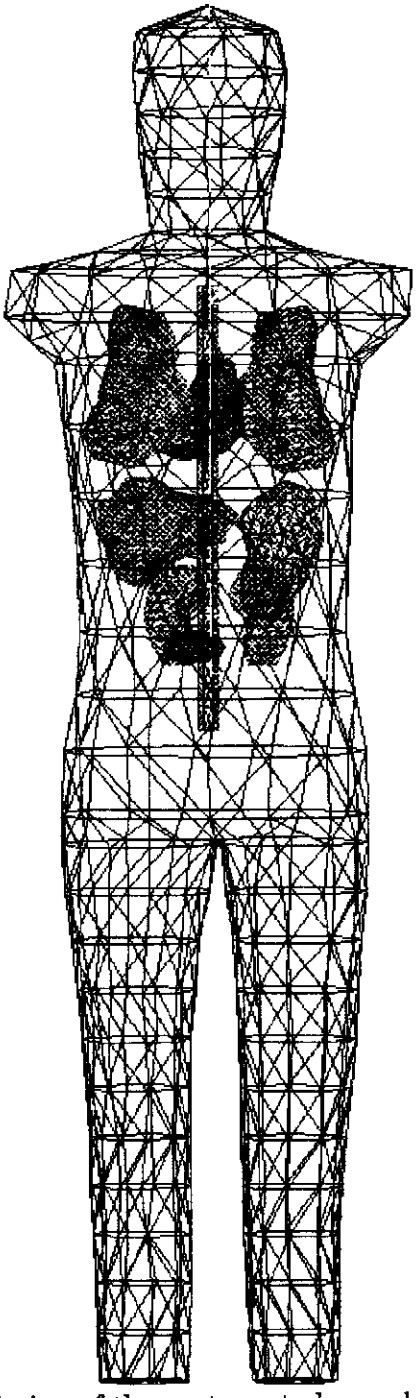

Figure 2: Boundary description of the anatomy to be meshed including internal organs and tissues which are electrically distinct. Geometry is derived from serial CT-scan data.

matrix) consumes 150 Mbytes of memory and run-times‡ increase by 11 Sec per BCG iteration. It is important to note that the anatomical model in Figs 2-3 does not yet contain a realistic representation of the body's skeleton. Reliable meshing of detailed skeletal structures has proved

‡ Processing the input data and performing the matrix and preconditioner assembly for a mesh of this size requires 30 minutes of CPU time

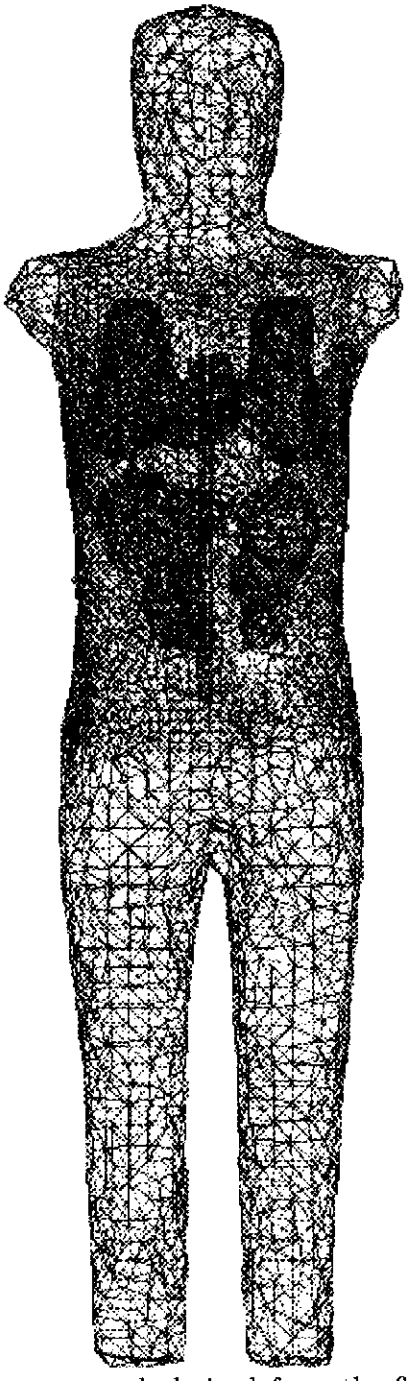

Figure 3: Actual boundary element mesh derived from the final volume element mesh generated to represent the anatomy specified in Fig 2. The boundaries produced conform to those of the original description given in Fig 2. Note the increased resolution of the body surface and internal organs relative to the original discretization in Fig 2.

to be beyond our present grid generation capabilities. Nonetheless, bony structures are important in many bioelectromagnetic applications because of their high electrical contrast relative to other soft tissues. Hence, it is imperative that we develop the ability to include relevant skeletal features

within our models in the future. Efforts along this dimension are currently underway.

V. Results

In this section we show some sample results of computed **H** and **E** distributions induced in the body model of Figure 3 by various noninvasive current source excitations. For convenience we enclose the body in a fictitious cylindrical boundary as shown in Figure 4 and enforce known current distributions over selected portions of the cylindrical surface which represent idealizations of physical devices used in hyperthermia treatment delivery. We handle the radiation fields away from the body by enclosing the model in $3 \times 3 \times 4$ meter region of equivalent dimensions to the shielded room in which most treatments of this type take place. On the outer boundary we require tangential **E** and normal **H** to vanish consistent with the nearly perfectly conducting nature of the walls of the treatment room. These conditions are implemented through the boundary integrals appearing in equation (2).

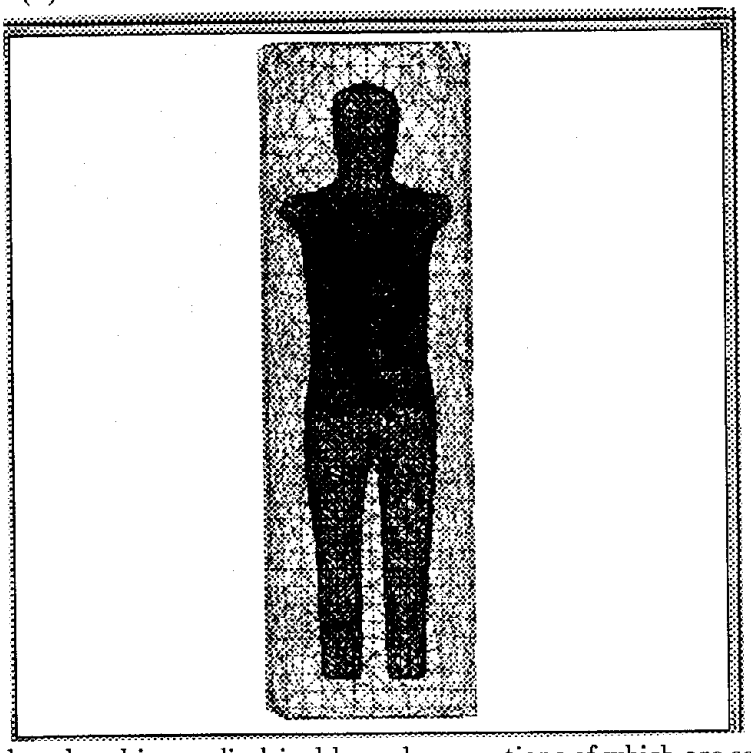

Figure 4: Body-model enclosed in a cylindrical boundary portions of which are selected to represent a noninvasive current source radiating EM fields into the body section of interest.

Specifically, we express (2) in a local normal/tangential coordinate system at nodes located on the walls. The first boundary integral in (2) vanishes identically since $\hat{\mathbf{n}} \times \mathbf{E}$ is assumed zero. The normal component of (2) is then discarded and the condition $H_n = 0$, consistent with $\hat{\mathbf{n}} \times \mathbf{E} = 0$, is enforced in its place as a Dirichlet condition on the primary field variable, **H**. The finite element grid is generated by meshing the exterior region and body simultaneously so that the tetrahedral elements which fill both the body and the space between the body and the treatment room walls conform to their common surface. In meshing the exterior region and body as a composite object, we begin with a 0.18m mesh spacing ($\approx$ 20 nodes per wavelength in air) and refine 4 times such that the internal organs have a 0.01125m characteristic nodal spacing. The electrical properties we use to simulate the various tissues and organs in our model are listed in Table 1.

In the first simulation example, we apply a uniform circumferential current which has a sinusoidal

dependence along a 100 cm length of the excitation surface described mathematically as

$$\mathbf{J} = \frac{1}{2}\left[1 + cos\left(\frac{\pi(2z - z_1 - z_2)}{z_2 - z_1}\right)\right]\hat{\phi} \tag{5}$$

where z_2 and z_1 are the top and bottom heights of the excitation source surface. This excitation is representative of magnetic induction hyperthermia [Sapozink *et. al.*, 1985, 1990] where the body section to be heated is placed inside a current-carrying concentric sheath. The frequency of excitation is 70MHz.

TABLE I: Tissue Electrical Properties

	ϵ_r	$\sigma\ (\Omega^{-1}m^{-1})$
Heart	72	0.89
Kidney	72	0.89
Liver	72	0.89
Lung	40	0.35
Muscle	66	0.593
Spine	10	0.20
Stomach	84	0.80
Tumor	72	0.89

Figure 5 shows the computed magnetic field distribution where the expected circulation of **H** around the current source is evident. In this figure the vector lengths as well as their gray level are proportional to their strength. Figure 6 displays the electric field derived by taking the curl of the numerical **H**. We achieve nodal values of **E** by performing a Galerkin treatment of $\mathbf{E} = \frac{1}{i\omega\epsilon^*}\nabla \times \mathbf{H}$ where we use nodal quadrature to avoid the inversion of an additional matrix as described elsewhere [Lynch *et. al.*, 1986]. The **E** solution circulates as anticipated and is largely confined to 2D cross-sections suggesting that simpler 2D analysis of this type of excitation may be sufficient for hyperthermia purposes.

The second simulation example shows computed **H** and **E** solutions for a current excitation polarized along the long axis of the body. Specifically, we select **J** to have the same sinusoidal dependence along the 100 cm length of the excitation surface as before, but also vary the circumferential magnitude sinusoidally such that

$$\mathbf{J} = \frac{1}{4}\left[1 + cos\left(\frac{\pi(2z - z_1 - z_2)}{z_2 - z_1}\right)\right]\left(1 + cos\frac{\phi}{8}\right)\hat{\mathbf{z}} \tag{6}$$

This idealization is representative of annular array applicators operating in the 70MHz range which are presently under investigation for noninvasive EM hyperthermia delivery [Sapozink *et. al.*, 1985, 1990]. The magnetic field is displayed in Figure 7 and its corresponding electric field in Figure 8. In this case the orientations of **H** and **E** are essentially reversed relative to the former simulation with **H** now circulating largely in cross-sectional planes and **E** oriented perpendicular to these cross-sections, but parallel to the long dimension of the body. The penetration of **E** within the body is greatly enhanced with this current source relative to the previous case. In Figure 9 we

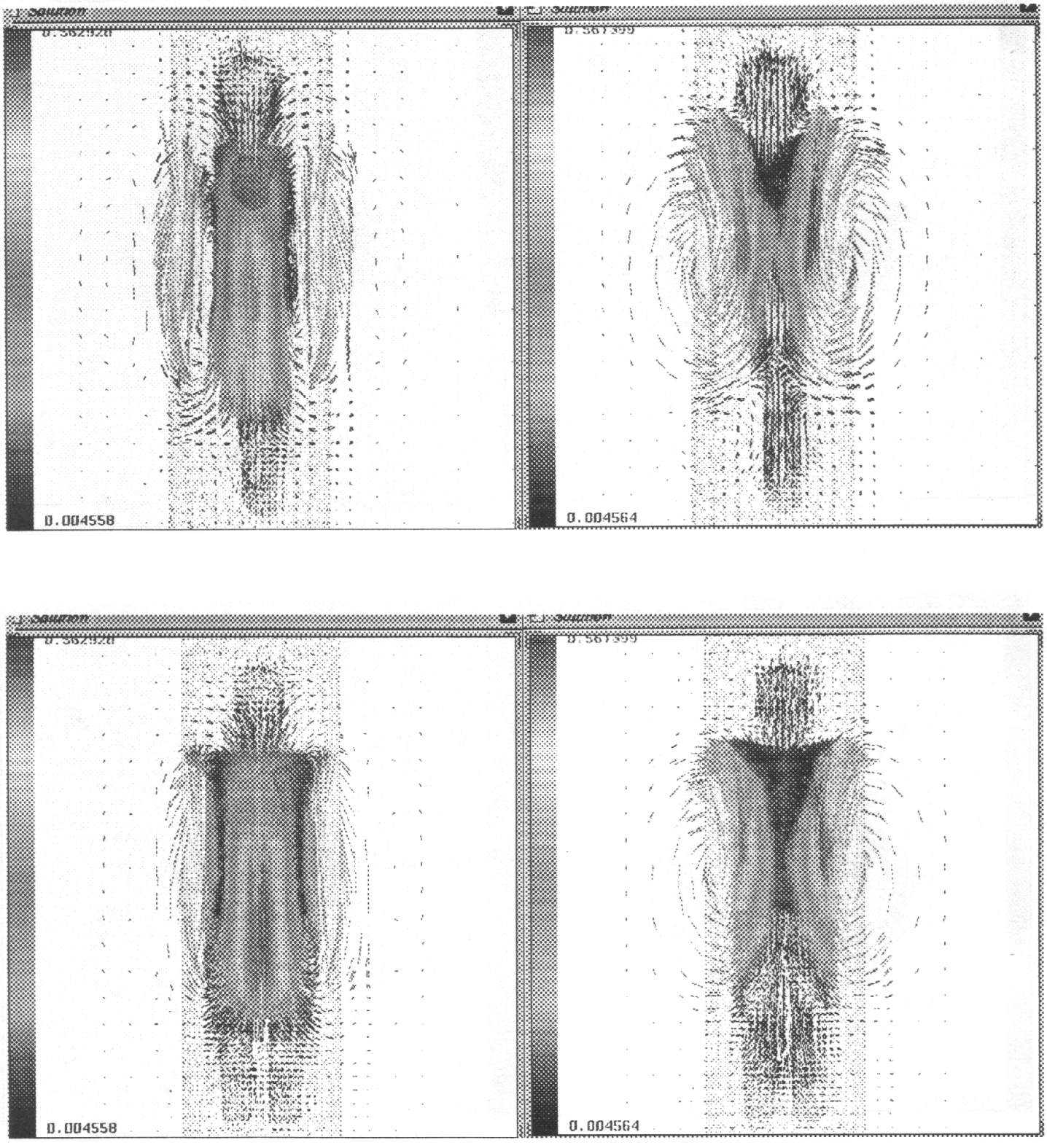

Figure 5. Computed $\mathbf{H}$ for the excitation given by equation (5) in the body model of Fig 4. Left: $Re(\mathbf{H})$, Right: $Im(\mathbf{H})$, Top: $x = 0$ plane, Bottom: $y = 0$ plane. Vector length and grey level are proportional to strength.

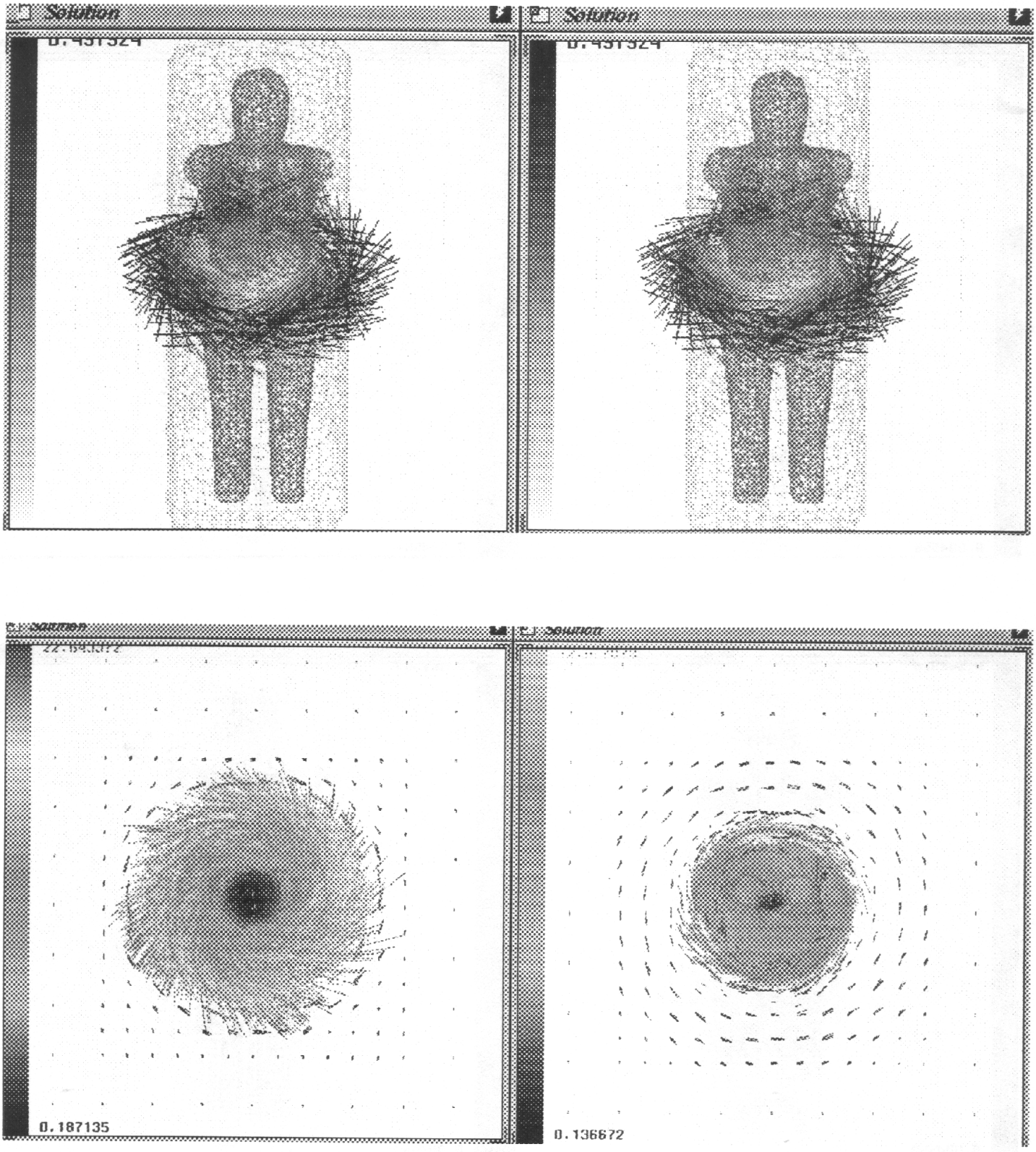

Figure 6: **E** solution computed from **H** in Fig 5

display only a subset of the overall vector solution in an attempt to highlight various features of

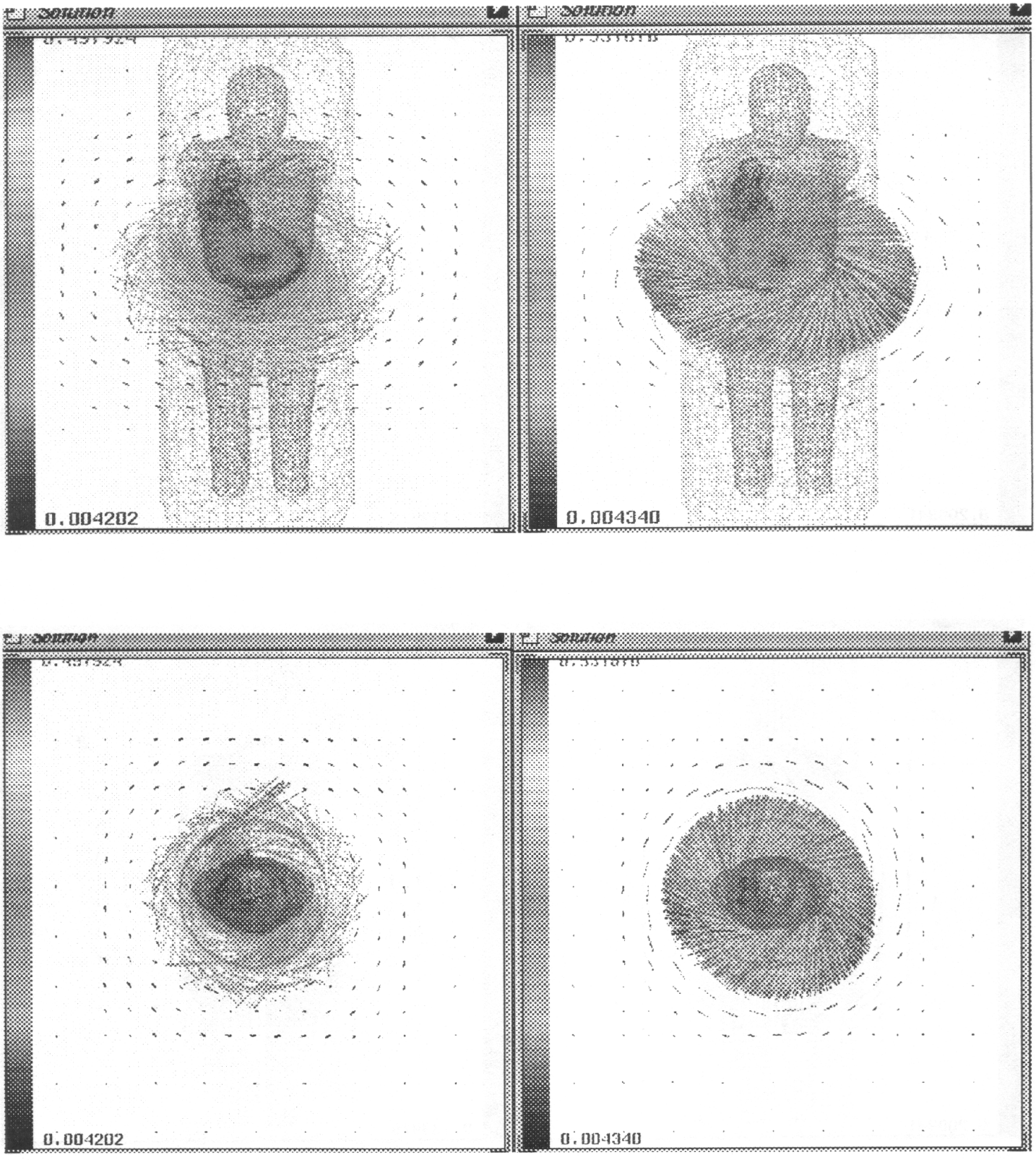

Figure 7. Computed **H** in the midplane of the current excitation given by equation (6) in the body model of Fig 4. Left: $Re(\mathbf{H})$, Right: $Im(\mathbf{H})$, Top: Front view, Bottom: End view. Vector length and grey level are proportional to strength.

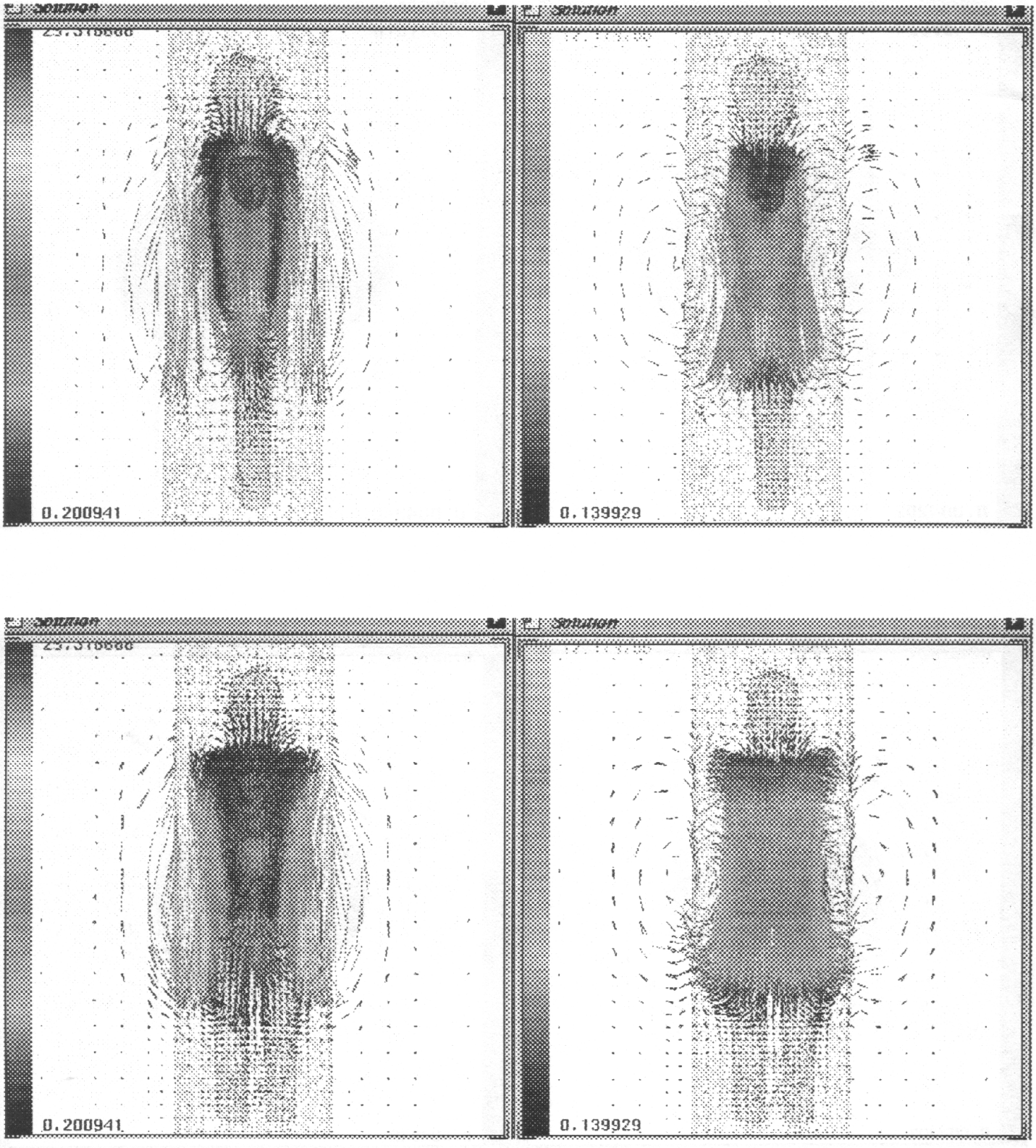

Figure 8. **E** solution computed from **H** in Fig 7. Top: $x = 0$ plane, Bottom: $y = 0$ plane.

the solution that one might be interested in. For example, it is interesting to note the phase change

in the **E** solution between the internal organs and the surrounding muscle tissue.

VI. Conclusions

We have demonstrated bioelectromagnetic computations on full-scale finite element man-models with significant levels of anatomical structure. Meshing is performed semi-automatically by developing a 3D boundary geometry of the region of interest from serial CT-scan data which is used as a template for guiding the creation of the final FEM grid. Irregular geometries and variable element sizes are possible such that the strength of the FEM is utilized in terms of providing flexibility in representing large computational domains. Sparse iterative matrix solution techniques allow problem sizes in excess of 100K degrees-of-freedom to be solved with run-times on the order of hours in the standard workstation computing environment.

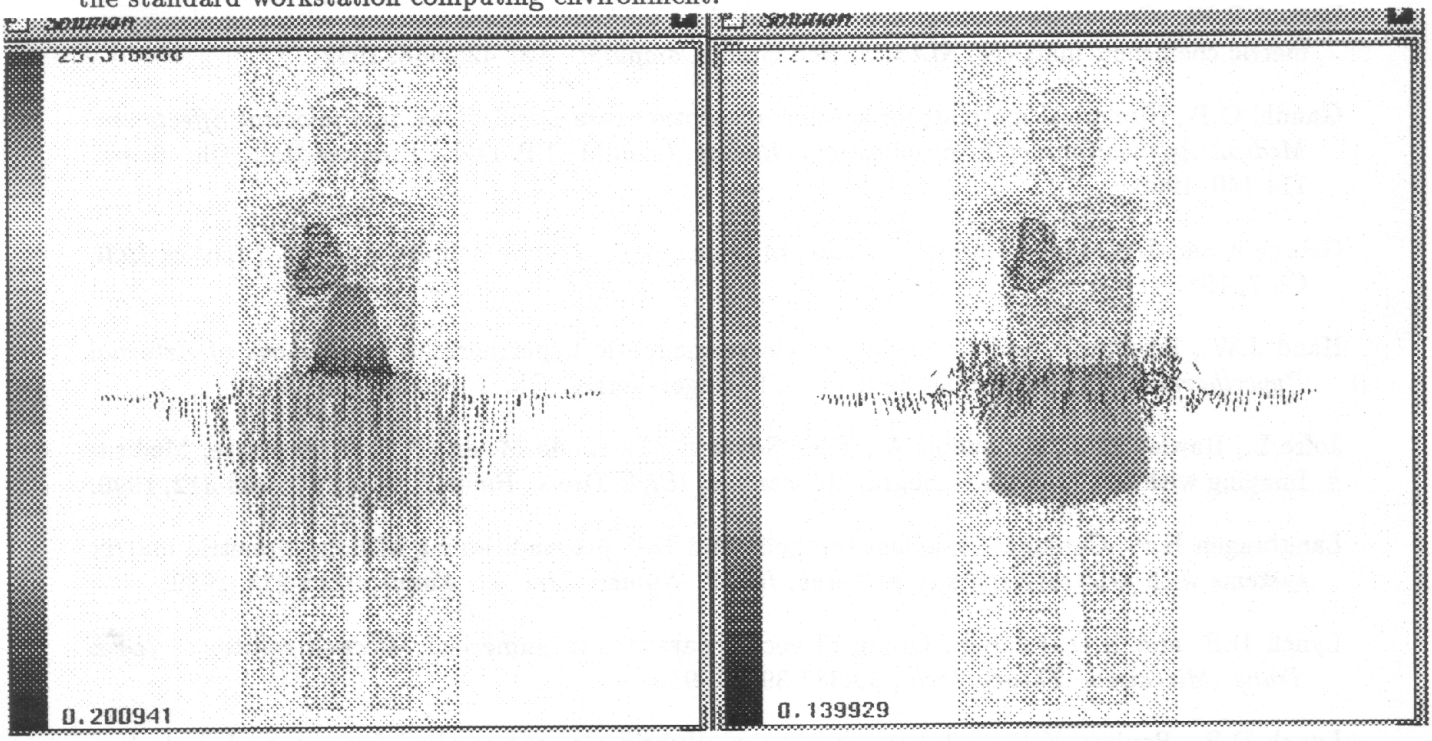

Figure 9. **E** solution in the midplane of the current excitation surface. The phase shift between the internal organs and the surrounding muscle tissue is evident.

Sample calculations in the hyperthermia cancer therapy context show that detailed **H** and **E** solutions are possible which highlight the salient features of EM interactions with electrically and geometrically distinct tissues and organs. Display of 3D vector data in an intelligible format is nontrivial and requires post-processing graphical routines which can plot solutions on subsets of the overall model (i.e. on arbitrarily-angled cutting planes through the geometry) or subsets of the overall collection of computed vectors (i.e. vectors within a prespecified magnitude range). In hyperthermia treatment planning, the ability to visualize specific anatomical structures and examine field phase and magnitude variations aids in the selection of source excitations which hopefully will lead to improved clinical hyperthermia delivery.

Acknowledgement: This work was supported in part by the National Institutes of Health Grants NIH/NCI CA37245 and CA45357.

References

Boyse W.E., Lynch D.R., Paulsen K.D., and G.N. Minerbo, Nodal based finite element modeling of Maxwell's equations in three dimensions, *IEEE Trans. Antennas Propagat* **40**:642-651, 1992.

Caorsi S., Gragnani G.L. and M. Pastorino, Equivalent current density reconstruction for microwave imaging purposes, *IEEE Microwave Theory Tech.*, **37**: 910-916, 1989.

Chen J.Y. and O.P. Gandhi, RF currents induced in an anatomically-based model of a human for plane-wave exposures 20-100MHz, *Health Phys.*, **57**: 89-98, 1989.

Freund R.W., Conjugate gradient type methods for symmetric linear systems with complex symmetric coefficient matrices, *SIAM J. Sci. Stat. Computat.*, **13**: 425-448, 1992.

Gandhi O.P., Numerical methods for specific absorption rate calculations, in *Biological Effects and Medical Applications of Electromagnetic Energy*, Gandhi O.P. (Ed), Prentice-Hall, Ch. 6, pp. 114-140, 1990.

George A and J.W. Liu, Computer solution of large sparse positive definite systems, *Prentice-Hall*, Ch 7, 1981.

Hand J.W., Biophysics and technology of electromagnetic hyperthermia, in *Methods of External Hyperthermic Heating*, M.Gautherie (Ed), Springer-Verlag, Ch. 1, pp. 1-60, 1990.

Jofre L., Hawley M.S., Broquetas A., delos Reyes E., Ferrando M. and A.R. Elias-Fuste, Medical Imaging with a microwave tomographic scanner, *IEEE Trans. Biomed. Eng.*, **37**: 303-312, 1990.

Langtangen H.P., Conjugate gradient methods and ILU preconditioning of nonsymmetric matrix systems with arbitrary sparsity patterns, *Int. J. Numer. Methods Fluids*, **9**213-233, 1989.

Lynch D.R. and K.D. Paulsen, Origin of vector parasites in numerical Maxwell solutions, *IEEE Trans. Microwave Theory Tech.*, **39**:383-394, 1991.

Lynch D.R., Paulsen K.D. and J.W. Strohbehn, Hybrid element method for unbounded electromagnetic problems in hyperthermia, *Int. J. Numer. Methods Eng*, **23**:1915-1937, 1986.

Lynch D.R., Paulsen K.D., Sullivan J.M., and J.W. Strohbehn, Hyperthermia analysis on finite elements, in *Proceedings of the 9th Annual Conference of the IEEE Engineering in Medicine and Biology Society*, pp. 1293-1295, 1987.

Medical Applications of Microwave Imaging, L.E. Larsen and J.H. Jacobi (Eds), IEEE Press, 1986.

Paulsen K.D., Calculation of power deposition patterns in hyperthermia, in *Thermal Modeling and Thermal Dosimetry*, M. Gautherie (Ed), Springer-Verlag, Ch. 2, pp. 57-118, 1990.

Paulsen KD and DR Lynch, Elimination of vector parasites in finite element Maxwell equation solutions, *IEEE Trans. Microwave Theory Tech.*, **39**: 395-404, 1991.

Paulsen K.D. and M.P. Ross, Comparison of numerical calculations with phantom experiments and clinical measurements, *Int. J. Hyperthermia*, **6**:333-349, 1990.

Paulsen K.D., Strohbehn J.W. and D.R. Lynch, Comparative theoretical performance for two types

of regional hyperthermia systems, *Int. J. Radiat. Oncol. Biol. Phys.*, **11**: 1659-1671, 1985.

Piket-May M.J., Taflove A., Lin W.C., Katz D.S., Sathiaseelan V., and B.B. Mittal, Initial results for automated computational modeling of patient-specific electromagnetic hyperthermia, **39**:226-237, 1992.

Sapozink M.D., Gibbs F.A., Thomason J.W., Eltringham J.R., and J.R. Stewart, A comparison of deep regional hyperthermia from an annular array and a concentric coil in the same patients, *Int. J. Rad. Oncol. Biol. Phys.*, **11**: 179-190, 1985.

Sapozink M.D., Joszef G., Astrahan M.A., Gibbs F.A., Petrovich Z, and J.R. Stewart, Adjuvant pelvic hyperthermia in advanced cervical carcinoma I. feasibility, thermometry and device comparison, *Int. J. Hyperthermia*, **6**:985-996, 1990.

Special Issue: Final Report of the NCI Hyperthermia Equipment Evaluation Contractor's Group, *Int. J. Hyperthermia*, 4:1-132, 1988.

Strohbehn J.W., Paulsen K.D. and D.R. Lynch, Use of finite element methods in computerized thermal dosimetry, in *Physical Techniques in Clinical Hyperthermia*, J.W. Hand and J.R. James (Eds), Research Studies Press, pp. 383-451, 1986.

Stuchly M.S. and SS Stuchly, Dielectric properties of biological substances – tabulated, *J Microwave Power*, **15**:19-26, 1980.

Sullivan D., Three-dimensional computer simulation in deep regional hyperthermia using the finite difference time domain method, *IEEE Trans. Microwave Theory Tech.*, **38**: 204-211, 1990.

Sullivan JM and G. Charron, 3D mesh generation system, *Numerical Methods Laboratory Report*, **NML 91-3**, Dartmouth College, Hanover, NH, 1991.

Yuan X. Lynch D.R. and K.D. Paulsen, Importance of normal field continuity in inhomogeneous scattering calculations, *IEEE Trans. Microwave Theory Tech.*, **39**:638-642, 1991.